Materials Today Communications 44 (2025) 112034

Contents lists available at ScienceDirect

Materials Today Communications

journal homepage: www.elsevier.com/locate/mtcomm

Phosphate coatings on WE43 magnesium alloy with improved corrosion resistance and bonding strength and effects of hydrothermal temperature

Yumeng Dong [a,b], Yanbin Zhao [a,b,d], Lei Yang [a,b], Juyi Yang [a,b], Jianwei Dai [a,b,e], Cheng Wang [a,b], Jing Bai [a,b,c], Feng Xue [a,b], Paul K. Chu [d], Chenglin Chu [a,b,*]

[a] School of Materials Science and Engineering, Southeast University, Nanjing 211189, China
[b] Jiangsu Key Laboratory for Advanced Metallic Materials, Southeast University, Nanjing 211189, China
[c] Institute of Medical Devices (Suzhou), Southeast University, Suzhou 215163, China
[d] Department of Physics, Department of Materials Science and Engineering, and Department of Biomedical Engineering, City University of Hong Kong, Hong Kong
[e] Jiangsu JITRI Surface Engineering Technology Research Institute, Taizhou, 225309, China

ARTICLE INFO

Keywords:
Magnesium alloy
Magnesium potassium phosphate coating
Corrosion resistance
Adhesion strength
Hydroxyapatite

ABSTRACT

Magnesium (Mg) alloys are promising orthopedic biomaterials due to their biocompatibility and degradability, but rapid and uncontrolled corrosion hampers clinical applications. In this study, magnesium potassium phosphate (MKP) coatings are prepared on the WE43 Mg alloy hydrothermally to improve the corrosion resistance and bonding strength. The influence of different conversion temperatures is evaluated. The MKP150 coating prepared at 150 °C is dense and free of cracks. Its corrosion rate (P_i, 0.07 mm·y^{-1}) and hydrogen evolution rate (HER, 7.9 × 10^{-4} mL·cm^{-2}·h^{-1}) are one order of magnitude lower than those of the bare Mg, and the corrosion current density (i_{corr}, 2.97 μA·cm^{-2}) decreases by 92.8 %. The hydrothermal temperature changes the corrosion resistance because it affects the critical nucleation radius and rate of MKP. The coating prepared at 150 °C has the optimal crystal size, thickness, shrinkage stress, as well as corrosion protection. On the other hand, microcracks are observed from the MKP180 coating deposited for a longer time. As a result of the *in situ* growth of the phosphate coating, the critical load of MKP150 reaches 7.05 N indicative of better adhesion strength. Coatings with high corrosion resistance and bonding strength on Mg alloys have large potential in clinical applications.

1. Introduction

Magnesium (Mg) and its alloys have received interest as orthopedic implant materials due to their biocompatibility and biodegradability [1,2], seeing that Mg is an essential element in maintaining the normal skeletal function. The elastic modulus and density of Mg-based implants are similar to those of human bone [3,4], thus reducing the stress shielding effect [5,6]. Moreover, Mg ions produced during degradation can also be absorbed without causing side effects [7]. However, the rapid degradation and subsequent release of hydrogen gas lead to premature failure and inflammatory responses [8,9], limiting the clinical applications of Mg alloys [10,11].

Surface modifications, such as micro-arc oxidation (MAO) [12], magnetron sputtering [13], chemical conversion coating [14,15], and electrodeposition [16], are capable of improving the corrosion resistance of Mg alloys. Hydrothermal treatment is a simple, cost-effective chemical conversion technique that can prepare coatings on Mg regardless of the substrate shape [17], making it ideal for orthopedic devices. Calcium- (Ca-) or Mg-phosphate (Ca-P or Mg-P) can be prepared hydrothermally, and Ca-P coatings have been shown to have favorable corrosion resistance and biocompatibility. However, cracks commonly found in Ca-P coatings reduce their service life [18,19]. Besides, the released Mg^{2+} prefers to form magnesium hydroxide to undermine the beneficial role of Ca^{2+} [17]. Hence, the limited adsorption sites for Ca-P nucleation and poor adhesion strength must be overcome.

Mg-P and its hydrates merit attention in the corrosion protection of Mg alloys because the substrate can act as reactants or precursors in coating formation [20,21]. Among them, magnesium phosphate potassium hexahydrate ($MgKPO_4·6H_2O$, MKP), has favorable resistance to dissolution, stability at an elevated temperature, and adjustable biodegradability. In our previous work [22], a biodegradable magnesium phosphate component (MPC) composed of MKP was produced and demonstrated to inhibit corrosion while improving cytocompatibility and osteogenic activity. Tang et al. [23] fabricated a bio-piezoelectric

* Corresponding author at: School of Materials Science and Engineering, Southeast University, Nanjing 211189, China.
E-mail address: clchu@seu.edu.cn (C. Chu).

https://doi.org/10.1016/j.mtcomm.2025.112034
Received 7 November 2024; Received in revised form 20 February 2025; Accepted 24 February 2025
Available online 28 February 2025

composite coating using MPC as the primary component, whose thickness exceeded 300 μm. However, MKP as a protective coating on Mg alloys has not yet been reported. This work employed the hydrothermal synthesis method to prepare a MKP coating on WE43 Mg alloys. The chemical reactions between magnesium oxide (MgO) and potassium dihydrogen phosphate (KH_2PO_4) improve the solubility of reactants [24], and by controlling the supersaturation temperature in the presence of high precursor concentrations, the nucleation process and crystal growth are promoted [25]. Herein, the effects of the hydrothermal treatment on the morphology and properties of MKP conversion coatings on the WE43 Mg alloy are determined to achieve the optimal performance.

2. Materials and methods

2.1. Materials

The WE43 Mg alloy provided by Suzhou Rongqian Rare Metal Product Co., Ltd. was cut into dimensions of 20 mm × 20 mm × 5 mm by wire cutting. Prior to the chemical conversion treatment, the samples were polished with silicon carbide (SiC) sandpapers up to 2000 grits, cleaned ultrasonically in anhydrous ethanol, and dried with warm air. Magnesium oxide (MgO, Mw: 40.3 $g{\cdot}mol^{-1}$, 98 %), potassium dihydrogen phosphate (KH_2PO_4, Mw: 136.1 $g{\cdot}mol^{-1}$, ≥ 99 %), and sodium hydroxide (NaOH, Mw: 40.0 $g{\cdot}mol^{-1}$, ≥ 99 %) were purchased from Sinopharm Chemical Reagent Co., Ltd. and used as-received.

2.2. Preparation

The fabrication process of the MKP coating is shown in Fig. 1. The clean substrates were alkalized with a 5 M NaOH solution at 60 °C for 2 h, rinsed with deionized water, and dried at 120 °C for 2 h. The solution for hydrothermal treatment was prepared by dissolving MgO and KH_2PO_4 in deionized water at 60 °C and stirred magnetically at 400 rpm for 30 min to obtain the Mg/P molar ratio of 1: 1. The pH of the suspension was controlled at 10, and then was transferred to a Teflon-liner autoclave in which the substrate was immersed in the solution. In the hydrothermal treatment, the samples were heated to 90, 120, 150, and 180 °C for 4 h (samples labeled as MKP90, MKP120, MKP150, and MKP180, respectively), rinsed, and dried at 37.5 °C for 12 h.

2.3. Characterization

Scanning electron microscopy (SEM, Nova Nano SEM450, USA) was used to examine the morphology of the MKP coatings. X-ray diffraction (XRD, Bruker D8-Discover, Germany) and Fourier transform infrared spectroscopy (FTIR, Thermo Scientific Nicolet iS10, USA) were carried out to determine the phase and chemical compositions of materials. XRD was performed in the 2θ range of 10°-80° with a step size of 0.25°.

2.4. Bonding strength

The adhesion strength of the MKP coatings was measured on the WS-2005 nano-scratch system. The scratches were observed under an optical microscope, and the images were recorded.

2.5. Corrosion properties

2.5.1. Electrochemical evaluation

The electrochemical corrosion properties were determined in Hank's balanced salt solution (HBSS) on an electrochemical workstation (PARSTAT, Princeton 3000, USA) with the standard three-electrode system with platinum as the counter electrode, a saturated calomel electrode as the reference electrode, and the sample (exposed area of 1 cm^2) as the working electrode. HBSS was composed of NaCl (8.0 $g{\cdot}L^{-1}$), KCl (0.4 $g{\cdot}L^{-1}$), $NaHCO_3$ (0.35 $g{\cdot}L^{-1}$), $MgCl_2{\cdot}6H_2O$ (0.1 $g{\cdot}L^{-1}$), $MgSO_4{\cdot}7\ H_2O$ (0.06 $g{\cdot}L^{-1}$), $CaCl_2$ (0.14 $g{\cdot}L^{-1}$), Na_2HPO_4 (0.06 $g{\cdot}L^{-1}$), KH_2PO_4 (0.06 $g{\cdot}L^{-1}$), and glucose (1 $g{\cdot}L^{-1}$). The open circuit potential (OCP) was determined to ensure that the working electrode reached a stable state. Electrochemical impedance spectroscopy (EIS) was conducted between 100 kHz and 0.1 Hz with a sinusoidal disturbance of 10 mV. The potentiodynamic polarization (PDP) curves were acquired at a scanning rate of 1 $mV{\cdot}s^{-1}$ in the potential range between −2.5 and −1.0 V/SCE. The corrosion current density (i_{corr}, $A{\cdot}cm^{-2}$) and potential (E_{corr}, V/SCE) were obtained by Tafel extrapolation of the cathodic branch of the polarization curve. The corrosion rate (P_i) was calculated by Eq. (1) [26]. The ZSimpWin software was employed in fitting the EIS results and deriving the equivalent circuits (ECs):

$$P_i = 22.85 i_{corr}. \quad (1)$$

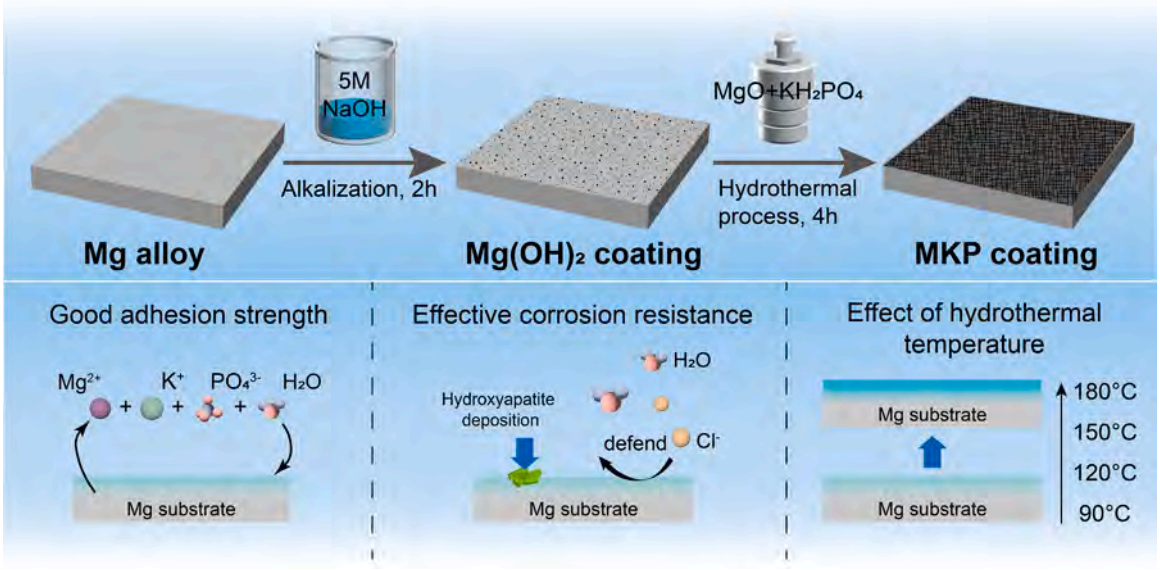

Fig. 1. Schematic diagram illustrating the preparation process and properties of MKP coatings on the WE43 Mg alloy.

2.5.2. Hydrogen evolution

To evaluate the long-term corrosion resistance, the samples were immersed in HBSS at 37.5 °C for 7 days. Hydrogen generated during corrosion was collected by a burette-funnel apparatus, and the pH of HBSS was recorded. The hydrogen evolution rate (v_H, mL·cm^{-2}·h^{-1}) was calculated by Eq. (2) [27]:

$$v_H = \frac{V}{st}, \quad (2)$$

where V is the cumulative hydrogen volume (mL), s is the exposed surface area (cm^2), and t is the immersion time (h).

2.5.3. Immersion test

The morphology and composition of the samples after immersion for 7 days were assessed by scanning electron microscopy (SEM) and energy-dispersive X-ray spectrometry (EDS). X-ray diffraction (XRD) and Fourier transform infrared (FTIR) spectroscopy were used to determine the composition of the corrosion products. The elemental composition and chemical states were analyzed by X-ray photoelectron spectroscopy (XPS, Thermo Scientific K-Alpha, USA).

3. Results

3.1. Characterization

Fig. 2 shows the morphologies of different MKP coatings prepared at different hydrothermal temperatures. All the samples exhibit flaky structures and grow oriented on the substrate. As shown in Fig. 2a-b, the samples prepared at low temperatures show low coverage. The plate-like structures agglomerated, creating weak areas in the coating. In contrast, MKP150 (Fig. 2c) shows a crack-free and dense surface with high coverage. However, if the hydrothermal temperature is too high, MKP180 has a loose flocculent morphology (Fig. 2d) which does not offer adequate protection to the substrate.

Fig. 3 displays the cross-sectional morphologies and EDS results. It is observed in EDS images that Mg, P, O, and K elements are uniformly distributed in the coating. With increasing hydrothermal temperature, the coating thicknesses change in the following order: MKP90 (3.1 μm) < MKP120 (4.8 μm) < MKP150 (6.3 μm) < MKP180 (14.8 μm). A high temperature fosters nucleation and precipitation of phosphate. The cross-section morphology becomes denser as the hydrothermal temperature is increased from 90 to 150 °C, but some cracks and holes appear from MKP180 due to internal stress [28]. In addition, there is no obvious interface between the MKP coating and substrate due to the *in situ* chemical conversion process.

Fig. 4a shows MKP and $Mg_3(PO_4)_2$·5 H_2O. With increasing temperature, the peak intensities of the phases strengthen, demonstrating enhanced coating stability at higher temperatures and greater thickness formation. These findings align with the EDS results. The peaks at 11.0° (020), 13.6° (110), and 23.2° (130) correspond to $Mg_3(PO_4)_2$·5H_2O. Fig. 4b reveals an absorption peak at 3450 cm^{-1} for the hydroxyl group, and those at 1073, 600, and 581 cm^{-1} correspond to the stretching and bending modes of phosphate [27]. The peak of H-O-H bending at 1645 cm^{-1} confirms the presence of crystalline water. These results indicate the successful deposition of MKP coatings on the Mg alloy.

3.2. Bonding strength

The adhesion strength between the coating and substrate is evaluated by the scratch test. The scratch images and corresponding critical fracture loads (L, N) of different samples are shown in Fig. 5 and Table 1. The L value of MKP150 is 7.05 N, representing 93.7 % and 17.9 % increases compared to MKP90 and MKP120, respectively. L increases with hydrothermal temperature, similar to the coating thickness.

3.3. Electrochemical characteristics

As shown in Fig. 6 and Table 2, the corrosion potential (E_{corr}) and current density (i_{corr}) are calculated by the Tafel extrapolation method. As the hydrothermal temperature goes up, E_{corr} rises in a positive direction (MKP90 (-1.74 V/SCE) < MKP120 (-1.69 V/SCE) < MKP150 (-1.56 V/SCE) < MKP180 (-1.48 V/SCE)). MKP150 shows obvious anodic passivity at voltages above E_{corr}. In contrast, the uncoated Mg exhibits typical active dissolution during anodic polarization [28]. Among the various samples, i_{corr} of MKP150 (2.97 μA·cm^{-2}) is the smallest, and P_i (0.07 mm·y^{-1}) is an order of magnitude lower than that of the Mg alloy (0.95 mm·y^{-1}), illustrating good corrosion resistance. And the electrochemical corrosion usually occurs on the interface of Mg and coating [29]. Therefore, MKP180 with microcracks provides better protection due to its sufficient thickness.

In the EIS plots (Fig. 7a-c), the semicircle in the high-frequency region is caused by the charge transfer resistance (R_{ct}) [30,31], and the low-frequency impedance modulus ($|Z|$) serves as a parameter to evaluate the corrosion resistance [32]. The largest diameter of the capacitive

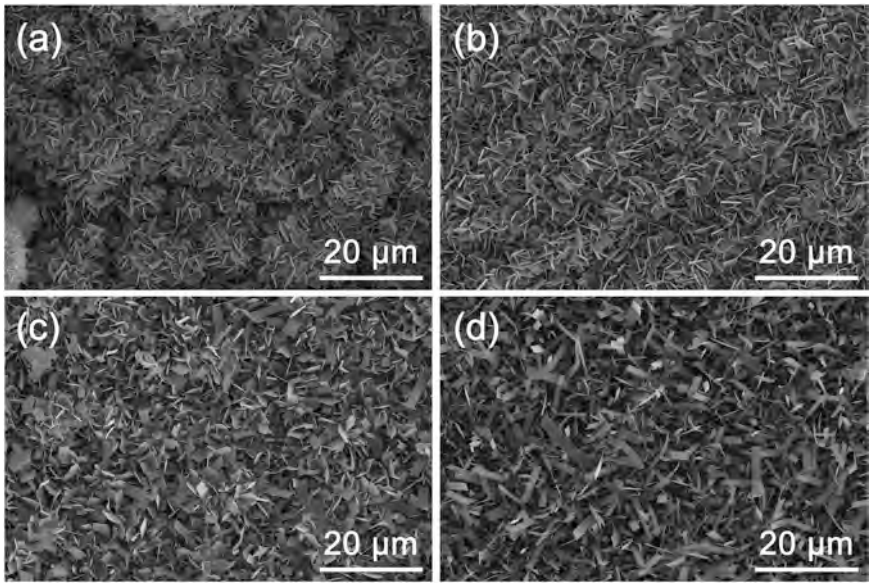

Fig. 2. Surface morphologies of (a) MKP90, (b) MKP120, (c) MKP150, and (d) MKP180.

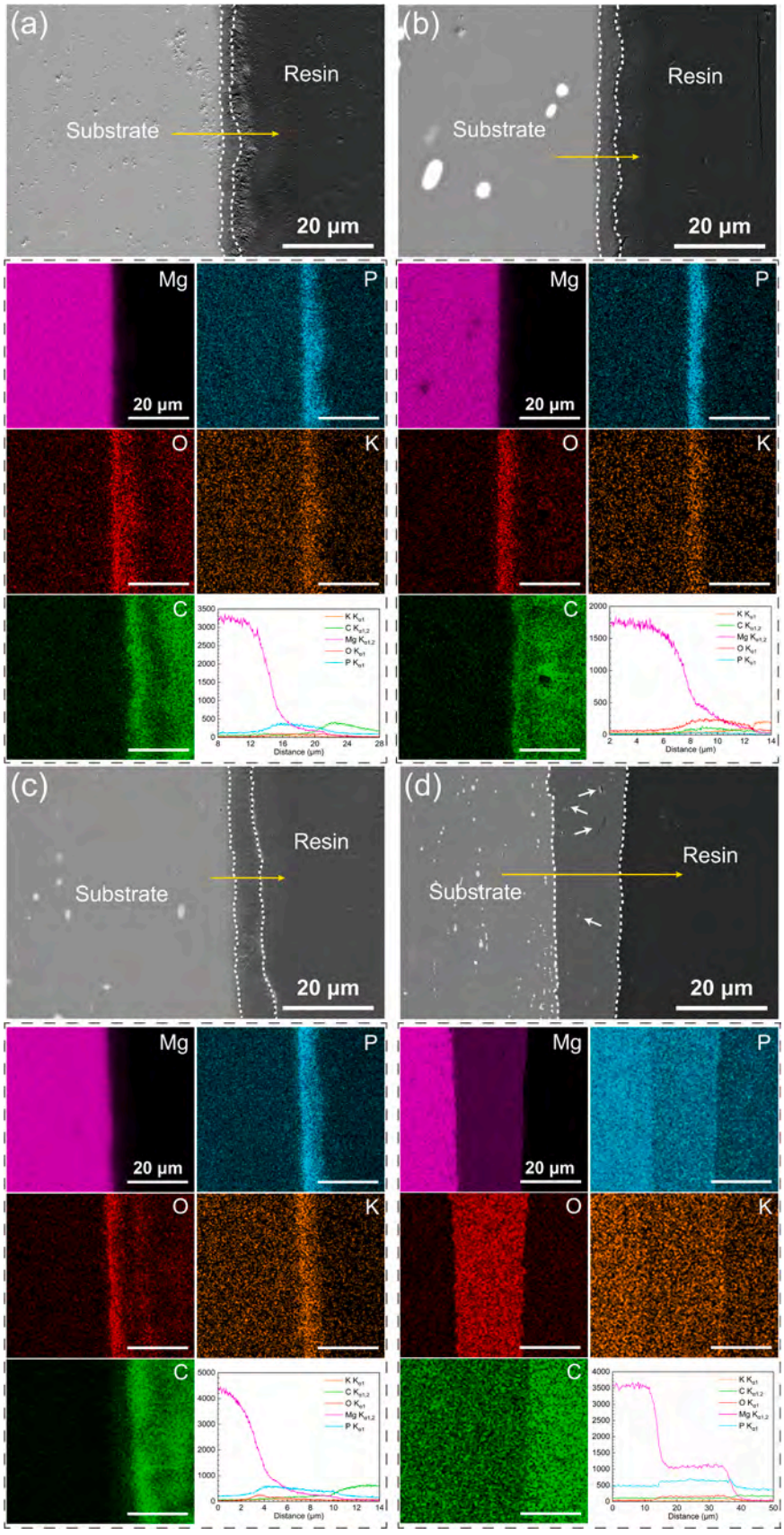

Fig. 3. Cross-sectional images and EDS maps of (a) MKP90, (b) MKP120, (c) MKP150, and (d) MKP180.

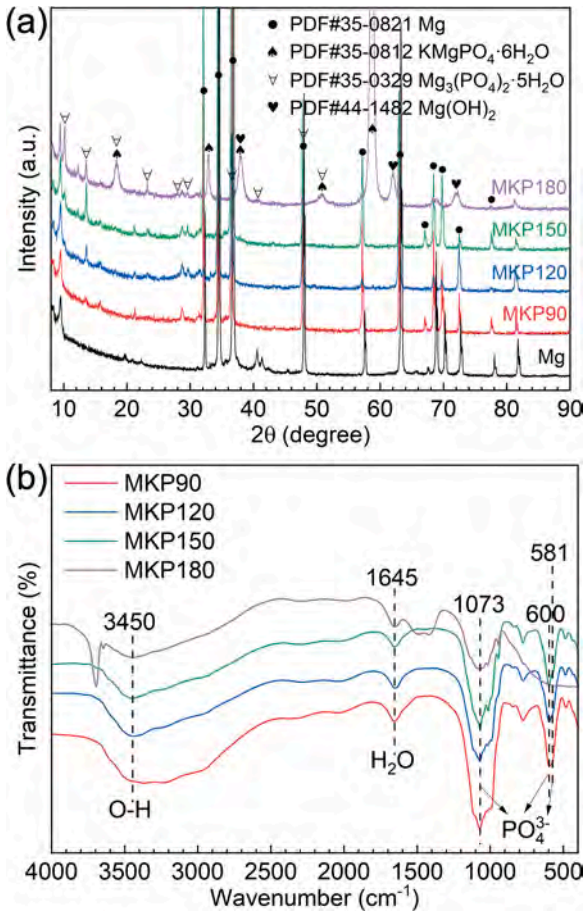

Fig. 4. (a) XRD patterns and (b) FTIR spectra of MKP coatings.

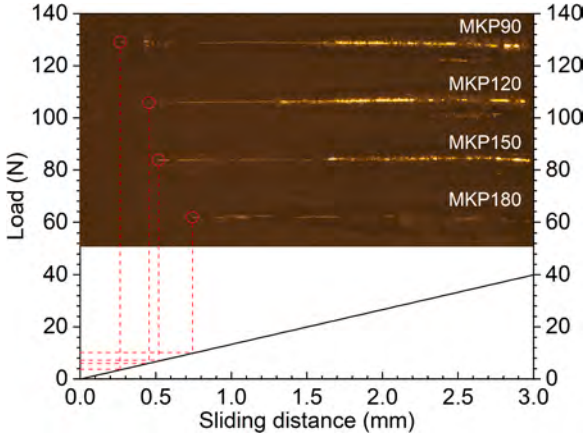

Fig. 5. Scratch test results of different MKP coatings.

Table 1
Critical loads obtained from scratch tests.

Sample	MKP90	MKP120	MKP150	MKP180
Load (N)	3.64	5.98	7.05	10.06

resistance arc of MKP150 represents better corrosion protection, which is corroborated by the SEM images in Figs. 2 and 3. The Bode diagram (Fig. 7b) shows that MKP150 has a larger impedance modulus at low frequencies of 0.1 Hz ($|Z|_{0.1\ Hz}$). The electrochemical results, including

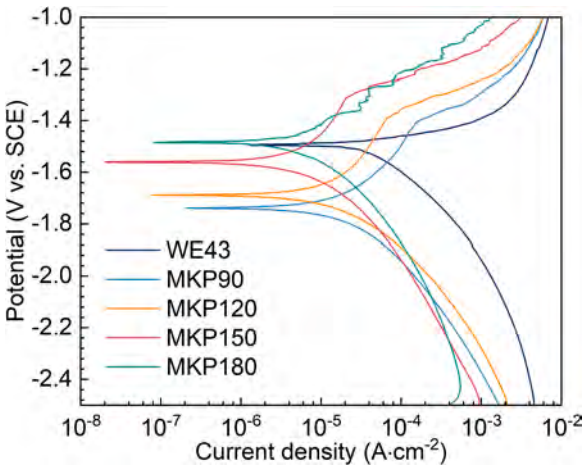

Fig. 6. Potentiodynamic polarization curves of bare Mg and different MKP coatings.

Table 2
Electrochemical parameters of the PDP curves in HBSS.

Samples	E_{corr} (V vs. SCE)	i_{corr} (μA·cm^{-2})	P_i (mm·y^{-1})
WE43	−1.49	41.5	0.95
MKP90	−1.74	12.9	0.30
MKP120	−1.69	8.43	0.19
MKP150	−1.56	2.97	0.07
MKP180	−1.48	3.68	0.08

low i_{corr} and high $|Z|_{0.1\ Hz}$, indicate that MKP150 has the best anti-corrosion properties [33].

To elucidate the corrosion mechanism in HBSS, two equivalent circuits (ECs) are derived from analyzing the EIS data, as shown in Fig. 7d-e. The important parameters derived from this analysis are listed in Table 3. In the circuits, R_s represents the solution resistance and R_{c1} and R_{c2} correspond to the resistances of the corrosive product film and MKP coating, respectively. A constant phase element (*CPE*, $Y_{CPE}(\omega) = 1/Z_{CPE} = Q_a(j\omega)^n$) [30]) is employed instead of a pure capacitor to compensate for the deviations caused by inhomogeneous surface reactions [34]. The *CPEs* are related to the corrosive product, conversion coating, and electrical double layer [35,36]. R_{ct} is inversely proportional to the degradation rate [37]. As shown in Table 3, R_{ct} (4556 Ω·cm^2) of MKP150 is the largest for improved protection against corrosion.

3.4. Hydrogen evolution

The hydrogen evolution rate (HER, mL·cm^{-2}·h^{-1}) is calculated by Eq. (1) and shown in Fig. 8, which reveals the following trend: Bare Mg (0.0055 mL·cm^{-2}·h^{-1}) > MKP90 (0.0046 mL·cm^{-2}·h^{-1}) > MKP180 (0.0041 mL·cm^{-2}·h^{-1}) > MKP120 (0.0008 mL·cm^{-2}·h^{-1}) > MKP150 (0.0007 mL·cm^{-2}·h^{-1}). In the first 4 h, the HER increases rapidly. For example, that of the bare Mg rises to three times that of the MKP coatings.

In the ensuing twenty hours, the corrosion rate declines gradually due to the formation and deposition of corrosion products such as the magnesium hydroxide ($Mg(OH)_2$) layer. Afterward, the corrosion rate remains relatively stable. Better protection is observed when the hydrothermal temperature is increased from 90 to 150 °C, but MKP180 exhibits an abnormal decrease in corrosion resistance. Because of the presence of micro-defects when the coating thickness becomes excessive, thereby allowing the corrosion medium to penetrate to the substrate. This is supported by the electrochemical results. Nevertheless, the HERs of all the coatings are less than that of the substrate.

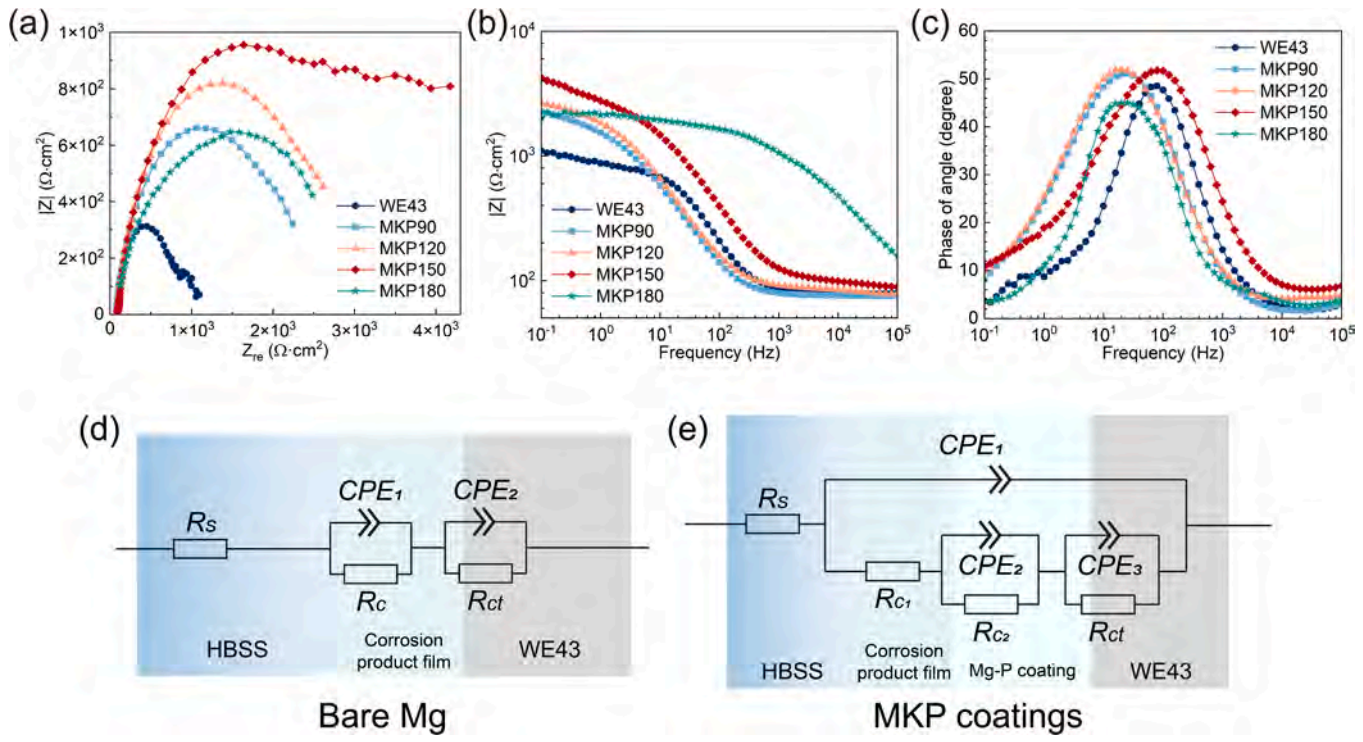

Fig. 7. Electrochemical measurements of different samples. (a) Nyquist plots, (b) Bode plots, and (c) Bode plot of phase angle vs. frequency; ECs of (d) WE43 and (e) MKP coatings.

Table 3
Fitted electrochemical parameters obtained by EIS simulation.

Samples	WE43	MKP90	MKP120	MKP150	MKP180
R_s (Ω·cm^2)	78.65	75.45	41.03	21.51	64.27
Y_1 (Ω^{-1}cm^{-2}s^{-1}×10^{-5})	92.64	3.671	8.970	8.299	0.0577
n_1	0.6600	0.8684	0.3465	0.2985	0.7129
R_{c1} (Ω·cm^2)	423.4	669.0	50.79	908.6	1277
Y_2 (Ω^{-1}cm^{-2}s^{-1}×10^{-5})	1.548	171.9	3.542	49.52	17.58
n_2	0.9228	0.8794	0.8465	0.9972	0.7412
R_{c2} (Ω·cm^2)	-	268.4	310.9	978.7	367.5
Y_3 (Ω^{-1}cm^{-2}s^{-1}×10^{-5})	-	10.84	1391	0.9113	0.7458
n_3	-	0.5712	0.6486	0.8561	0.5801
R_{ct} (Ω·cm^2)	602.6	1379	3286	4556	1470

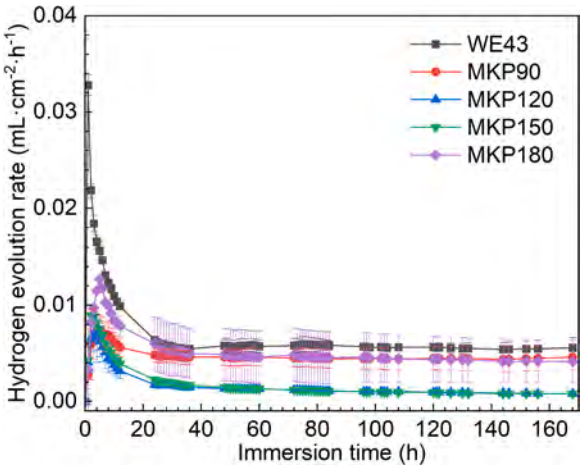

Fig. 8. HER curves of bare Mg and MKP coatings during immersed in HBSS for 7 days.

3.5. Degradation behavior

The SEM morphologies and EDS results of the immersed samples are shown in Fig. 9a-d. After 7 days of immersion, the bare Mg alloy shows grid-like cracks and even fragmentation. Compared with other MKP-coated samples, MKP150 remains intact with few defects. On the contrary, MKP90, MKP120, and MKP180 fail to block corrosive ions due to pits and cracks. With regard to MKP150, more corrosion products are present on the broken coating, whereas there are many agglomerated particles on MKP180. EDS indicates that the products after immersion mainly consist of magnesium phosphate and calcium phosphate. The Ca/P ratio is less than 1 in most areas, which can be attributed to the possible incorporation of Mg^{2+} during the nucleation and growth process of apatite [29]. The corrosion resistance and stability of MKP150 were confirmed by morphology and EDS results after 14 days of immersion, as shown in the Supplementary Materials. The MKP150 still maintained complete coverage with minimal corrosion product deposition. Spherical products appeared abundantly on the surface of bare Mg and other MKP-coated samples. The Ca/P ratio calculated from Fig. S1 (e2) point p1 was 1.48, which is closer to the stoichiometric ratio of hydroxyapatite (HAp). The substrate of these specimens was exposed and cracked to varying degrees.

XRD and FTIR are used to characterize the corrosion products after immersion in HBSS for 7 days. As shown in Fig. 10a, the peaks at 22.8° (111), 31.8° (211), and 32.9° (300) correspond to HAp . In the FTIR spectra in Fig. 10b, the band at 1073 cm^{-1} represents the stretching modes of PO_4^{3-}, while that at 581 cm^{-1} arises from bending of PO_4^{3-}. The peak at 580–600 cm^{-1} representing P-O vibration in HAp becomes broader and stronger [38]. The peak of O-H bending of crystalline water at 1645 cm^{-1} is the same in both spectra. These results demonstrate that the MKP coatings promote the formation of HAp in HBSS [39].

The chemical composition of the corrosion products is analyzed by XPS. As shown in Fig. 11, Mg 1 *s*, O 1 *s*, Ca 2*p*, K 2*p*, C 1 *s*, Cl 2*p*, and P 2*p* are detected from the corroded MKP150 coating. The Mg 1 *s* spectrum exhibits Mg-OH (1303.08 eV), Mg-O (1303.88 eV), and Mg-PO_4^{3-} (1304.78 eV). The O 1 *s* spectrum of the hybrid coating shows C═O/C-O

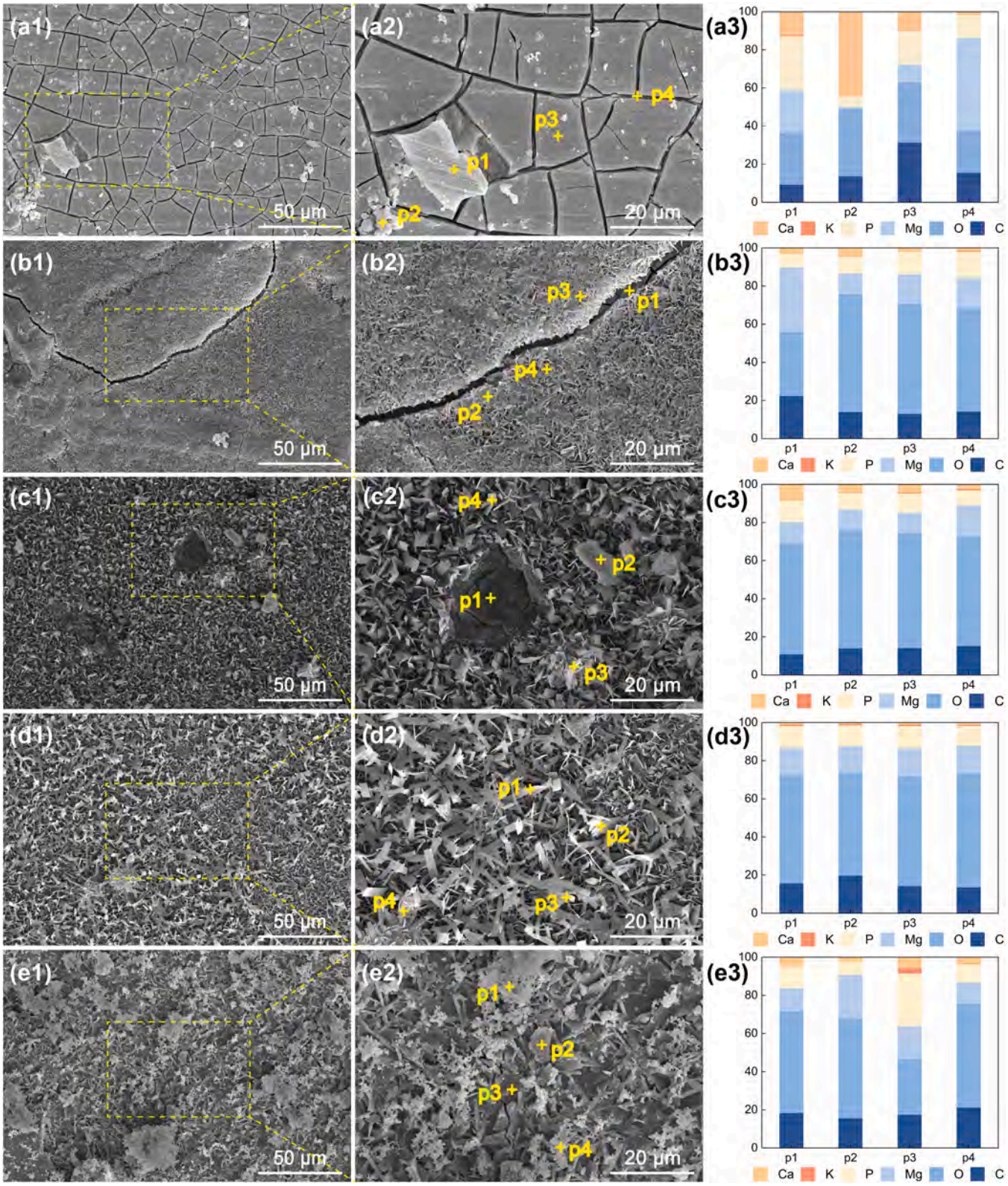

Fig. 9. SEM images and corresponding EDS results of (a1-a3) bare Mg, (b1-b3) MKP90, (c1-c3) MKP120, (d1-d3) MKP150, and (e1-e3) MKP180 after immersion in HBSS for 14 days.

(532.78 eV), Mg-O (531.48 eV), and -OH (530.68 eV). The Ca 2*p* spectrum confirms the formation of Ca-P products during corrosion, similar to XRD and FTIR [40]. The P 2*p* spectrum reveals the existence of HPO_4^{2-} (133.98 eV) and PO_4^{3-} (132.78 eV). The results suggest that corrosion leads to the formation of HAp, which is expected to improve the bioactivity [41].

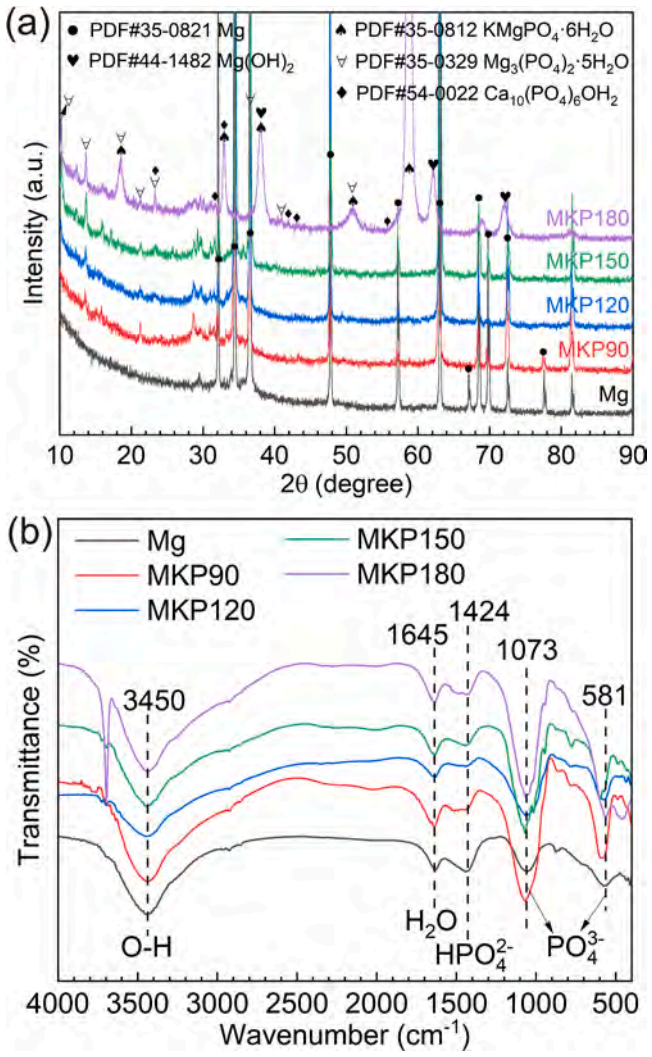

Fig. 10. (a) XRD patterns and (b) FTIR spectra of the samples immersed in HBSS for 7 days.

4. Discussion

4.1. Formation mechanism

Fig. 12 describes the formation process of the coatings. Firstly, the Mg substrate was alkalized to achieve surface activation. The hydroxyl group on the surface induces the deposition of potassium, phosphate, and other ions from the solution [42]. At the same time, the $Mg(OH)_2$ layer serves as a source of Mg and provides dense nucleation sites for the formation of MKP. The hydrothermal treatment enhances the solubility of MgO, shifting the equilibrium toward the formation of MKP and uniform nucleation. The flaky MKP nucleates, expands, and covers the entire surface to impede ion penetration, giving rise to the surface morphology in Fig. 2.

During the formation process, the hydrothermal temperature modulates the MKP coating morphology by changing the thermodynamic equilibrium, solubility, and nucleation free energy. The Gaussian function, often known as the nucleation function, can be used to approximate the final mean particle size and size distribution of MKP [43]. Ideally, increasing the maximum nucleation rate (Γ_{max}) results in a smaller average crystal size, while minimizing the nucleation time window (Δt_n) allows for a narrower size distribution. Γ_{max} is primarily influenced by two factors, one of which is the critical nucleation radius r_c, calculated by:

$$r_c = -\frac{2\sigma T_0}{\Delta H_m \Delta T}, \tag{3}$$

where σ is the interfacial energy between the crystal nucleus and parent phase, T_0 is the nucleation temperature, ΔH_m is the enthalpy change, and ΔT is the difference between the actual and theoretical nucleation temperature. The other factor is the nucleation rate I_n, which is calculated by:

$$I_n \approx \frac{Nk_BT}{h}\exp\left(-\frac{\Delta G^*}{RT}\right)\exp\left(-\frac{16\pi\sigma^3 T_0^2}{3RT(\Delta H_m \Delta T)^2}\right), \tag{4}$$

where N is the number of atoms per unit volume, k_B is Boltzmann's constant, T is the actual temperature, h is the Planck constant, ΔG^* is the barrier to be crossed over for the atom transition from the parent phase to the nucleus, and R is the molar gas constant. Based on the theory, the rise of hydrothermal temperature raises ΔT, which in turn increases r_c and I_n, while Δt becomes relatively larger. In consequence, the thickness of the MKP coating increases. However, when the hydrothermal temperature was raised to 180 °C, the rapid coating growth rate led to internal stress accumulation. The increased coating thickness prevents these stresses from being released during subsequent cooling and drying processes. As a result, MKP180 exhibited microcracks within the coating and reduced corrosion resistance. Evidently, an appropriate hydrothermal temperature is necessary to form a dense and uniform coating. Furthermore, owing to the gradient change of N, the coating has fine and compact grains close to the surface of the substrate to provide better corrosion protection.

4.2. Corrosion mechanism

The corrosion mechanism of the MKP-coated Mg in HBSS is proposed in Fig. 13. With regard to the MKP coatings, K-struvite degrades in HBSS to a certain extent because of the following reaction [23]:

$$MgKPO_4{\cdot}6H_2O \rightarrow Mg^{2+} + K^+ + PO_4^{3-} + 6H_2O. \tag{5}$$

The corrosion medium then propagates and further destroys the coating, resulting in exposed substrate and accelerated corrosion [44]:

$$\text{Anodic reaction}: Mg \rightarrow Mg^{2+} + 2e^- \tag{6}$$

$$\text{Cathodic reaction}: 2H_2O + 2e^- \rightarrow 2OH^- + H_2\uparrow \tag{7}$$

$$\text{General reaction}: Mg + 2H_2O \rightarrow Mg(OH)_2 + H_2\uparrow \tag{8}$$

After local degradation, the ingress of Cl^- converts the protective product $Mg(OH)_2$ to soluble magnesium chloride shown below [45]:

$$Mg(OH)_2 + 2Cl^- \rightarrow MgCl_2 + 2OH^- \tag{9}$$

Hence, the concentration of OH^- in HBSS increases, and $H_2PO_4^-$ and HPO_4^{2-} ions are converted into PO_4^{3-} as shown below:

$$H_2PO_4^- + OH^- \rightarrow HPO_4^{2-} + H_2O \tag{10}$$

$$HPO_4^{2-} + OH^- \rightarrow PO_4^{3-} + H_2O. \tag{11}$$

Thus, the local saturation of Ca^{2+}, OH^-, HPO_4^{2-}, and PO_4^{3-} increased at the pitting or solution interfaces [46]. Furthermore, the ions combine to form HAp to maintain the surface charge:

$$10Ca^{2+} + 10HPO_4^{2-} + 12OH^- \rightarrow Ca_{10}(PO_4)_6(OH)_2 + 10H_2O + 4PO_4^{3-} \tag{12}$$

$$10Ca^{2+} + 6PO_4^{3-} + 2OH^- \rightarrow Ca_{10}(PO_4)_6(OH)_2 \tag{13}$$

Based on the EDS results in Fig. 9, the Ca/P ratio in the area with severe corrosion is larger, proving that corrosion of Mg and MKP produces HAp [47]. Moreover, excess Mg^{2+} and PO_4^{3-} in the solution combine to form magnesium phosphate shown below:

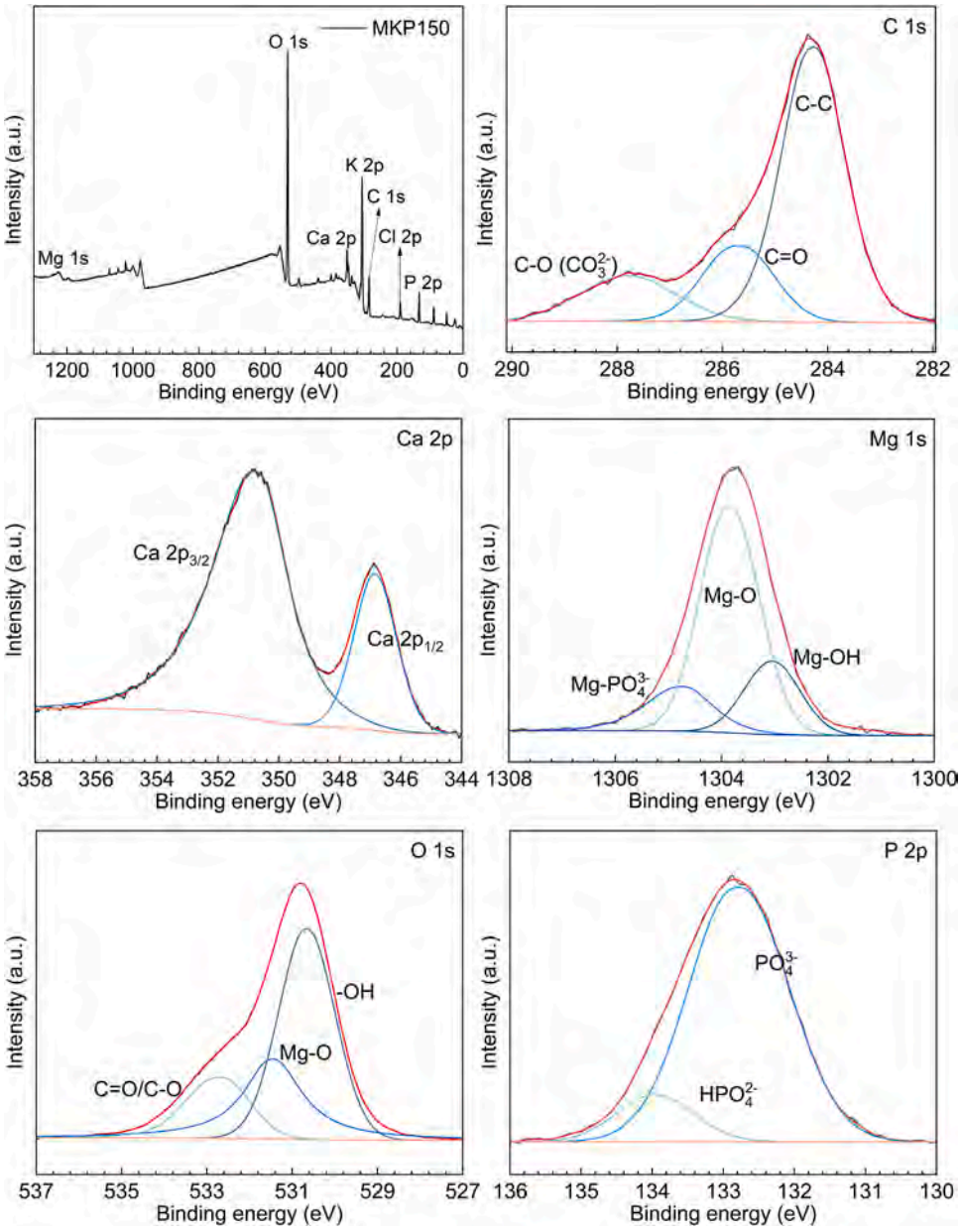

Fig. 11. XPS spectra of MKP150 sample after 7-day immersion.

$$3Mg^{2+} + 2PO_4^{3-} \rightarrow Mg_3(PO_4)_2 \quad (14)$$

In summary, the main corrosion precipitates are $Mg(OH)_2$ and $Ca_{10}(PO_4)_6(OH)_2$, which can be confirmed by the XRD patterns (Fig. 10). Furthermore, the corrosion products also can be used as physical barrier to protect Mg alloy from corrosion.

4.3. Comparison of corrosion resistance and adhesion strength

The i_{corr} values are summarized in Fig. 14. Liu et al. [48] have reported that despite pretreating the WE43 substrate by a filtered cathodic vacuum arc (FCVA) to increase nucleation sites, the phosphate coating still exhibits obvious cracks. Wang et al. [49] have tried to improve the loose structure of the single Ca-P coating by introducing chitosan (CS), but the corrosion resistance is still limited (i_{corr}, 4.98 μA·cm^{-2}). In this study, dense MKP coatings are prepared by a hydrothermal method. Compared to other studies shown in Fig. 14, our sample shows a 92.8 % reduction in i_{corr} relative to the bare Mg alloy of only 2.97 μA·cm^{-2}. These findings suggest that hydrothermal conversion of MKP coatings on Mg alloys is a promising anti-corrosion approach.

Fig. 15 compares the bonding strength of different Ca-P coatings on Mg alloys. Traditional Ca-P coatings usually have poor adhesion, coarse grains, high porosity, and limited degradation resistance. This is because Mg^{2+} competes with Ca^{2+} by forming $Mg(OH)_2$ [17]. Yang et al. [39] have attempted to address the lattice mismatch caused by this competitive mechanism by applying a composite polymer coating, but their results indicate that further improvement is necessary. Herein, a hydrothermal treatment is designed to promote the *in situ* growth of MKP. The cross-sectional morphology and EDS results in Fig. 3 confirm that the MKP coating adheres firmly to the substrate without an obvious interface. Consequently, in the scratch test, the MKP150 coating shows a critical load of 7.05 N, which is higher than that (< 5 N) reported in other studies, as shown in Fig. 15.

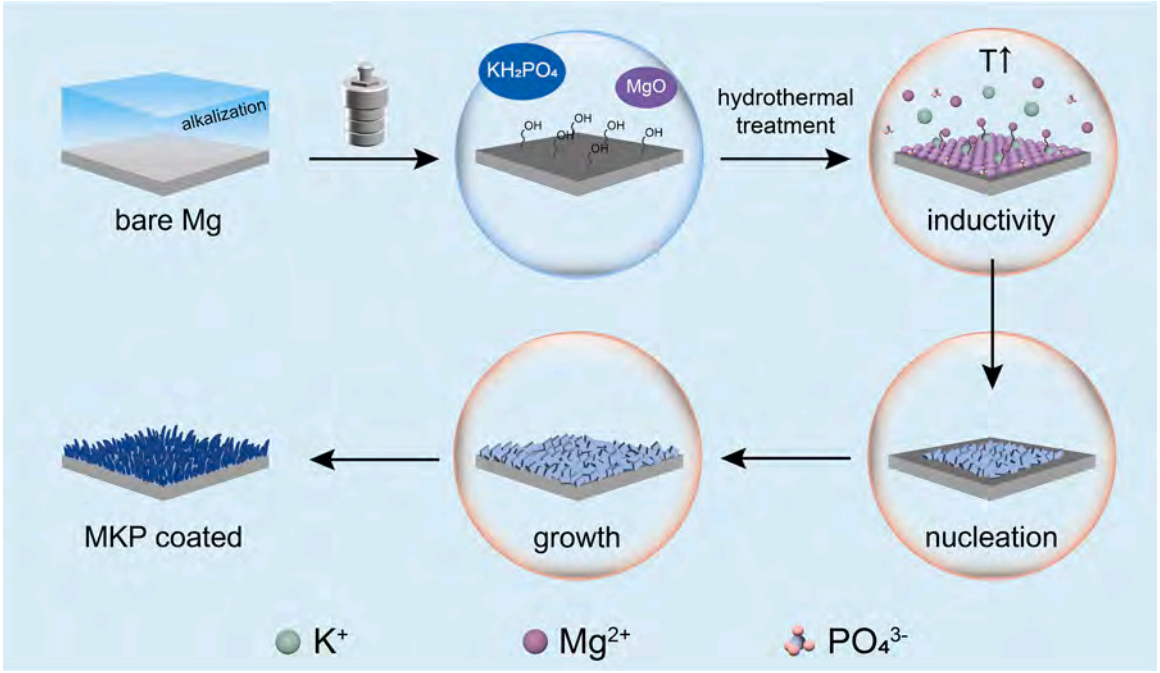

Fig. 12. Schematic diagram of the MKP coating formation process.

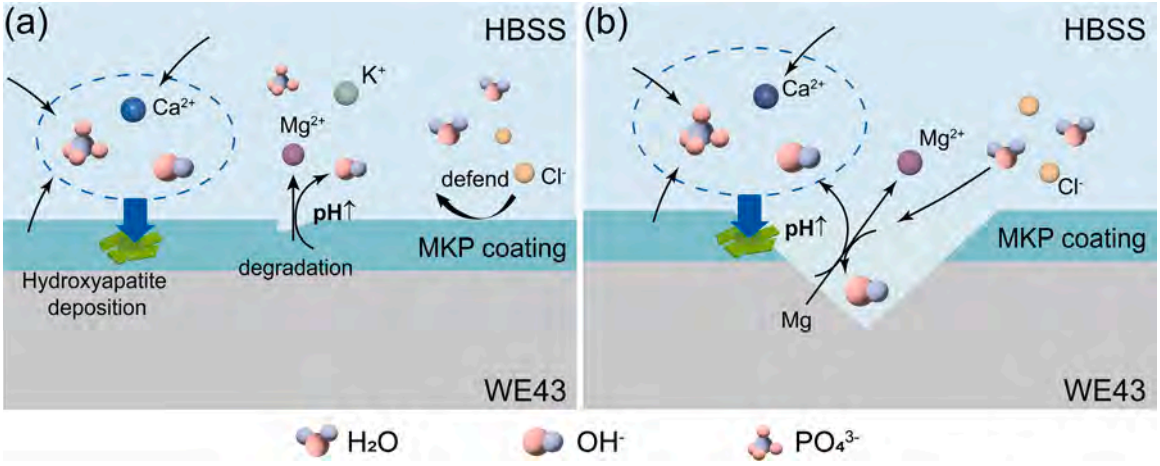

Fig. 13. Corrosion mechanism of the MKP coated Mg alloy system.

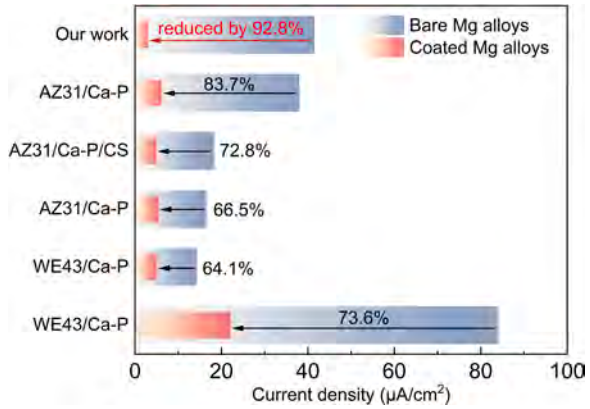

Fig. 14. Comparison of i_{corr} with other reported Ca-P coatings [39,48–51].

5. Conclusion

A magnesium potassium phosphate (MKP) coating with improved corrosion resistance and bonding strength is prepared by a hydrothermal process. The 6.3 μm thick MKP150 coating prepared at 150 °C exhibits a defect-free morphology and no obvious interface with the substrate. The corrosion current density (i_{corr}, 2.97 μA·cm^{-2}) and hydrogen evolution rate (HER, 7.9 × 10^{-4} mL·cm^{-2}·h^{-1}) of MKP150 are an order lower than those of bare Mg, in addition to excellent bonding strength due to the *in situ* growth of phosphate, manifested by a critical load of 7.05 N in the scratch test. The optimal temperature of 150 °C produces a dense morphology and optimal internal stress because of the moderate growth rate. The corrosion resistance is improved because the MKP coating facilitates the formation of the Ca-P film, especially hydroxyapatite (HAp).

CRediT authorship contribution statement

Dong Yumeng: Writing – review & editing, Writing – original draft,

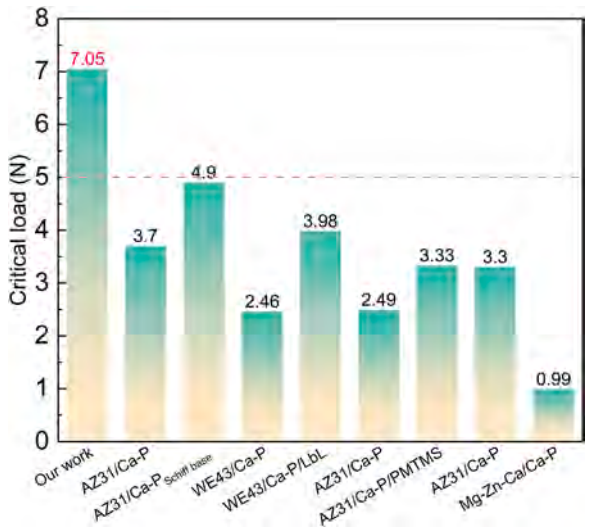

Fig. 15. Comparison of the critical loads in the scratch tests of different samples [39,51–54].

Software, Methodology, Formal analysis, Conceptualization. **Zhao Yanbin**: Validation, Investigation, Data curation. **Yang Lei**: Visualization, Software, Investigation. **Yang Juyi**: Writing – review & editing, Methodology. **Dai Jianwei**: Visualization, Software. **Wang Cheng**: Resources. **Xue Feng**: Resources. **Bai Jing**: Resources. **Chu Paul K.**: Writing – review & editing, Resources. **Chu Chenglin**: Supervision, Project administration, Conceptualization.

Declaration of Competing Interest

The authors declare that they have no known competing financial interests or personal relationships that could have appeared to influence the work reported in this paper.

Acknowledgments

This work was supported by the National Natural Science Foundation of China (Grant number 52171236), State Key Program of the National Natural Science Foundation of China (Grant number 52231005), Open Research Fund of Jiangsu Key Laboratory for Advanced Metallic Materials, Southeast University (Grant number AMM2024A01), Suzhou Science and Technology Project (Grant numbers SJC2023005 and SZS2023023), City University of Hong Kong Strategic Research Grant (SRG) (Grant number 7005505), as well as City University of Hong Kong Donation Research Grant (Grant number DON-RMG 9229021).

Appendix A. Supporting information

Supplementary data associated with this article can be found in the online version at doi:10.1016/j.mtcomm.2025.112034.

Data Availability

The data that has been used is confidential.

References

[1] L. Yang, Y. Lai, K. Yue, Y. Liu, H. Jin, Corrosion research and fractal characteristics of As-cast and semisolid AZ91D magnesium alloys, Corrosion 79 (2023) 762–770.
[2] Y. Zhao, P. He, B. Wang, J. Bai, F. Xue, C. Chu, Incorporating pH/NIR responsive nanocontainers into a smart self-healing coating for a magnesium alloy with controlled drug release, bacteria killing and osteogenesis properties, Acta Biomater. 174 (2024) 463–481.
[3] S. Shaikh, I. Qayoom, R. Sarvesha, A. Kumar, Bioresorbable magnesium-based alloys containing strontium doped nanohydroxyapatite promotes bone healing in critical sized bone defect in rat femur shaft, J. Magnes. Alloy. 11 (2023) 270–286.
[4] H. Zhou, B. Liang, H. Jiang, Z. Deng, K. Yu, Magnesium-based biomaterials as emerging agents for bone repair and regeneration: from mechanism to application, J. Magnes. Alloy. 9 (2021) 779–804.
[5] F. Badkoobeh, H. Mostaan, M. Rafiei, H.R. Bakhsheshi-Rad, S. RamaKrishna, X. Chen, Additive manufacturing of biodegradable magnesium-based materials: design strategies, properties, and biomedical applications, J. Magnes. Alloy. 11 (2023) 801–839.
[6] X. Gu, Y. Li, C. Qi, K. Cai, Biodegradable magnesium phosphates in biomedical applications, J. Mater. Chem. B 10 (2022) 2097–2112.
[7] J. Zhang, Y. Jiang, Z. Shang, B. Zhao, M. Jiao, W. Liu, M. Cheng, B. Zhai, Y. Guo, B. Liu, X. Shi, B. Ma, Biodegradable metals for bone defect repair: a systematic review and meta-analysis based on animal studies, Bioact. Mater. 6 (2021) 4027–4052.
[8] X. Ma, W. Huang, Z. Niu, W. Li, D. Mei, S. Zhu, S. Guan, A drug-loaded bio-functional anticorrosion coating on Mg alloy for orthopedic applications, Mater. Lett. 311 (2022) 131581.
[9] Y. Zhao, J. Bai, F. Xue, R. Zeng, G. Wang, P.K. Chu, C. Chu, Smart self-healing coatings on biomedical magnesium alloys: a review, Smart Mater. Manuf. 1 (2023) 100022.
[10] J. Nachtsheim, S. Ma, J. Burja, B.Š. Batič, B. Markert, Tuning the long-term corrosion behaviour of biodegradable WE43 magnesium alloy by PEO coating, Surf. Coat. Technol. 474 (2023) 130115.
[11] Q. Dong, J. Jiang, J. Zhang, Z. Hu, X. Zhang, Clarifying stress corrosion cracking behavior of biomedical Mg-Gd-Zn-Zr alloy, J. Magnes. Alloy. (2024).
[12] L. Qian, M. Sun, N. Huang, P. Yang, F. Jing, A. Zhao, B. Akhavan, Biodegradable PTMC-MAO composite coatings on AZ31 Mg-alloys for enhanced corrosion-resistance, J. Alloy. Compd. 998 (2024) 175017.
[13] L. Dragomir, A. Antoniac, V. Manescu, A. Robu, M. Dinu, I. Pana, C.M. Cotrut, E. Kamel, I. Antoniac, J.V. Rau, A. Vladescu, Preparation and characterization of hydroxyapatite coating by magnetron sputtering on Mg–Zn–Ag alloys for orthopaedic trauma implants, Ceram. Int. 49 (2023) 26274–26288.
[14] X. Li, E. Lin, K. Wang, R. Ke, S.-Z. Kure-Chu, X. Xiao, Fabrication and characterization of hydroxyapatite coatings on anodized magnesium alloys by electrochemical and chemical methods intended for biodegradable implants, Ceram. Int. 50 (2024) 36838–36848.
[15] F. Zhang, C. Zhang, L. Song, R. Zeng, S. Li, H. Cui, Fabrication of the superhydrophobic surface on magnesium alloy and its corrosion resistance, J. Mater. Sci. Technol. 31 (2015) 1139–1143.
[16] J.E. Park, Y.S. Jang, S.Y. Kim, J.B. Choi, T.S. Bae, I. Park, M.H. Lee, Corrosion properties and biocompatibility of strontium doped calcium phosphate coated magnesium prepared by electrodeposition, Mater. Today Commun. 31 (2022).
[17] L. Ling, S. Cai, Q. Li, J. Sun, X. Bao, G. Xu, Recent advances in hydrothermal modification of calcium phosphorus coating on magnesium alloy, J. Magnes. Alloy. 10 (2022) 62–80.
[18] X. Wang, X. Liu, Y. Dai, J. She, D. Zhang, F. Qi, W. Wei, X. Ouyang, A novel Ca-Mg-P/PDA composite coating of Mg alloys to improve corrosion resistance for orthopedic implant materials, Surf. Coat. Technol. 471 (2023) 129920.
[19] Y. Song, S. Zhang, J. Li, C. Zhao, X. Zhang, Electrodeposition of Ca–P coatings on biodegradable Mg alloy: in vitro biomineralization behavior, Acta Biomater. 6 (2010) 1736–1742.
[20] H. Zhao, S. Cai, Z. Ding, M. Zhang, Y. Li, G. Xu, A simple method for the preparation of magnesium phosphate conversion coatings on a AZ31 magnesium alloy with improved corrosion resistance, RSC Adv. 5 (2015) 24586–24590.
[21] P.Mohan Sathyaraj, K. Ravichandran, T.Sankara Narayanan, Controlling the rate of degradation of Mg using magnesium fluoride and magnesium fluoride-magnesium phosphate duplex coatings, J. Magnes. Alloy. 10 (2022) 314–331.
[22] Y. Zhao, Y. Li, B. Wang, J. Yao, Y. Fan, P. He, J. Bai, C. Wang, F. Xue, C. Chu, An injectable magnesium-based cement stimulated with NIR for drug-controlled release and osteogenic potential, Adv. Healthc. Mater. 13 (2024) 2400207.
[23] Y. Tang, L. Zhu, P. Zhang, K. Zhao, Z. Wu, Enhanced corrosion resistance of bio-piezoelectric composite coatings on medical magnesium alloys, Corros. Sci. 176 (2020) 108939.
[24] L. Yu, K. Xia, C. Gong, J. Chen, W. Li, Y. Zhao, W. Guo, H. Dai, An injectable bioactive magnesium phosphate cement incorporating carboxymethyl chitosan for bone regeneration, Int. J. Biol. Macromol. 160 (2020) 101–111.
[25] M. Willinger, M. Felhofer, E. Reimhult, R. Zirbs, Method for high-yield hydrothermal growth of silica shells on nanoparticles, Materials 14 (2021) 6646.
[26] Z.M. Shi, M. Liu, A. Atrens, Measurement of the corrosion rate of magnesium alloys using Tafel extrapolation, Corros. Sci. 52 (2010) 579–588.
[27] Y.B. Zhao, P. He, J.Y. Yao, M. Li, B. Wang, L.Y. Han, Z.H. Huang, C. Guo, J. Bai, F. Xue, Y. Cong, W.H. Cai, P.K. Chu, C.L. Chu, pH/NIR-responsive and self-healing coatings with bacteria killing, osteogenesis, and angiogenesis performances on magnesium alloy, Biomaterials 301 (2023) 122237.
[28] G. Guo, D. Song, J. Jiang, A. Ma, L. Zhang, C. Li, Effect of synthesizing temperature on microstructure and electrochemical property of the hydrothermal conversion coating on Mg-2Zn-0.5Mn-Ca-Ce alloy, Metals 6 (2016) 44.
[29] C. Zhang, J. Zhang, S. Zhang, Z. Wang, Comparison of calcium phosphate coatings on AZ31 and fluoride-treated AZ31 alloy prepared by hydrothermal method and their electrochemical corrosion behaviour, Mater. Chem. Phys. 220 (2018) 395–401.
[30] L. Zhang, X. Zhang, J. Dai, J. Yang, J. Bai, Z. Huang, C. Guo, F. Xue, L. Han, C. Chu, Effects of different magnitudes of static stress on the in vitro corrosion behavior of biodegradable zinc, Corros. Sci. 227 (2024) 111763.

[31] M. Razavi, M. Fathi, O. Savabi, D. Vashaee, L. Tayebi, In vitro study of nanostructured diopside coating on Mg alloy orthopedic implants, Mater. Sci. Eng. C - Mater. 41 (2014) 168–177.
[32] J.M. Zhang, X. Duan, A.R. Hou, J.C. Li, K. Wang, H. Cai, In situ preparation of Mg-Al-Co layered double hydroxides on microarc oxidation ceramic coating of LA103Z Magnesium-lithium alloy for enhanced corrosion resistance, J. Mater. Eng. Perform. 30 (2021) 8490–8499.
[33] Q. Dong, Z. Ba, Y. Jia, Y. Chen, X. Lv, X. Zhang, Z. Wang, Effect of solution concentration on sealing treatment of Mg-Al hydrotalcite film on AZ91D Mg alloy, J. Magnes. Alloy. 5 (2017) 320–325.
[34] M.S. Palanisamy, R. Kulandaivelu, S.N.T.S. Nellaiappan, Improving the corrosion resistance and bioactivity of magnesium by a carbonate conversion-polycaprolactone duplex coating approach, N. J. Chem. 44 (2020) 4772–4785.
[35] C.H.M. Beraldo, A. Versteg, A. Spinelli, N. Scharnagl, T.F. da Conceição, Anticorrosive properties of chitosan-derivatives coatings on Mg AZ31 alloy in Hank's Balanced Salt Solution, Int. J. Biol. Macromol. 260 (2024) 129390.
[36] W. Zai, X. Zhang, Y. Su, H.C. Man, G. Li, J. Lian, Comparison of corrosion resistance and biocompatibility of magnesium phosphate (MgP), zinc phosphate (ZnP) and calcium phosphate (CaP) conversion coatings on Mg alloy, Surf. Coat. Technol. 397 (2020) 125919.
[37] X. Fu, W. Du, H. Dou, Y. Fan, J. Xu, L. Tian, J. Zhao, L. Ren, Nanofiber composite coating with self-healing and active anticorrosive performances, ACS Appl. Mater. Interfaces 13 (2021) 57880–57892.
[38] R. Ellerbrock, M. Stein, J. Schaller, Comparing amorphous silica, short-range-ordered silicates and silicic acid species by FTIR, Sci. Rep. 12 (2022).
[39] J. Yang, Y. Zhao, J. Dai, L. Han, Q. Dong, L. Zhang, J. Bai, F. Xue, P.K. Chu, C. Chu, Fabrication and growth mechanism of multilayered hydroxyapatite/organic composite coatings on the WE43 magnesium alloy, Surf. Coat. Technol. 452 (2023) 129125.
[40] S. Liao, J. Bai, X. Xia, X. Liao, Y. Zhang, Q. Deng, F. Dong, The insight into behavior and mechanism of chitosan-embedded hydroxyapatite gel spheres used for efficient solidification of uranium in wastewater, J. Ind. Eng. Chem. (2024).
[41] D. He, X. Zhang, P. Liu, X. Liu, X. Chen, F. Ma, W. Li, K. Zhang, H. Zhou, Effect of hydrothermal treatment temperature on the hydroxyapatite coatings deposited by electrochemical method, Surf. Coat. Technol. 406 (2021) 126656.
[42] Weiyang Lv, Ji'an Sun, Y. Yao, Morphology control of layered double hydroxide and its application in water remediation, Prog. Chem. 32 (2020) 2049–2063.
[43] Z. Li, J. Yang, T. Guang, B. Fan, K. Zhu, X. Wang, Controlled hydrothermal/solvothermal synthesis of high-performance LiFePO4 for Li-ion batteries, Small Methods 5 (2021) 2100193.
[44] J. Niu, G. Yuan, Y. Liao, L. Mao, J. Zhang, Y. Wang, F. Huang, Y. Jiang, Y. He, W. Ding, Enhanced biocorrosion resistance and biocompatibility of degradable Mg-Nd-Zn-Zr alloy by brushite coating, Mater. Sci. Eng. C Mater. Biol. Appl. 33 (2013) 4833–4841.
[45] A. Zhang, P. Lenin, R. Zeng, M. Bobby Kannan, Advances in hydroxyapatite coatings on biodegradable magnesium and its alloys, J. Magnes. Alloy. 10 (2022) 1244–1263.
[46] Y. Pan, S. He, D. Wang, D. Huang, T. Zheng, S. Wang, P. Dong, C. Chen, In vitro degradation and electrochemical corrosion evaluations of microarc oxidized pure Mg, Mg–Ca and Mg–Ca–Zn alloys for biomedical applications, Mater. Sci. Eng. C. -Mater. 47 (2015) 85–96.
[47] M.H. Salimi, J.C. Heughebaert, G.H. Nancollas, Crystal growth of calcium phosphates in the presence of magnesium ions, Langmuir 1 (1985) 119–122.
[48] X. Liu, X. Wang, L. Ren, Y. Dai, J. She, F. Qi, W. Wei, D. Zhang, X. Ouyang, Improved deposition quality of calcium-phosphate coating on the surface of WE43 magnesium alloy via FCVA sputtering pretreatment, J. Mater. Res. Technol. 26 (2023) 6672–6688.
[49] L. Wang, X. Xiao, X. Yin, J. Wang, G. Zhu, S. Yu, E. Liu, B. Wang, X. Yang, Preparation of robust, self-cleaning and anti-corrosion superhydrophobic Ca-P/chitosan (CS) composite coating on AZ31 magnesium alloy, Surf. Coat. Technol. 432 (2022) 128074.
[50] P. Liu, J.M. Wang, X.T. Yu, X.B. Chen, S.Q. Li, D.C. Chen, S.K. Guan, R.C. Zeng, L. Y. Cui, Corrosion resistance of bioinspired DNA-induced Ca-P coating on biodegradable magnesium alloy, J. Magnes. Alloy. 7 (2019) 144–154.
[51] X.M. Wang, X.L. Fan, M.Q. Zeng, C.Y. Li, L.Y. Cui, X.B. Chen, Y.H. Zou, Z.L. Wang, R.C. Zeng, In vitro degradation resistance of glucose and L-cysteine-bioinspired Schiff-base anodic Ca-P coating on AZ31 magnesium alloy, T. Nonferr. Metal. Soc. 32 (2022) 1485–1500.
[52] L. Cao, L. Wang, L. Fan, W. Xiao, B. Lin, Y. Xu, J. Liang, B. Cao, RGDC peptide-induced biomimetic calcium phosphate coating formed on AZ31 magnesium alloy, Materials 10 (2017) 358.
[53] D. Chen, D. Mei, L. Chen, C. Wang, J. Bai, F. Xue, C. Chu, L. Wang, S. Zhu, S. Guan, A ceria/calcium-phosphate functional composite coating on magnesium alloy for enhanced adhesion strength, corrosion resistance, and biocompatibility, Appl. Surf. Sci. 672 (2024) 160790.
[54] Y.B. Zhao, L.Q. Shi, L.Y. Cui, C.L. Zhang, S.Q. Li, R.C. Zeng, F. Zhang, Z.L. Wang, Corrosion resistance of silane-modified hydroxyapatite films on degradable magnesium alloys, Acta Metall. Sin. -Engl. Lett. 31 (2018) 180–188.

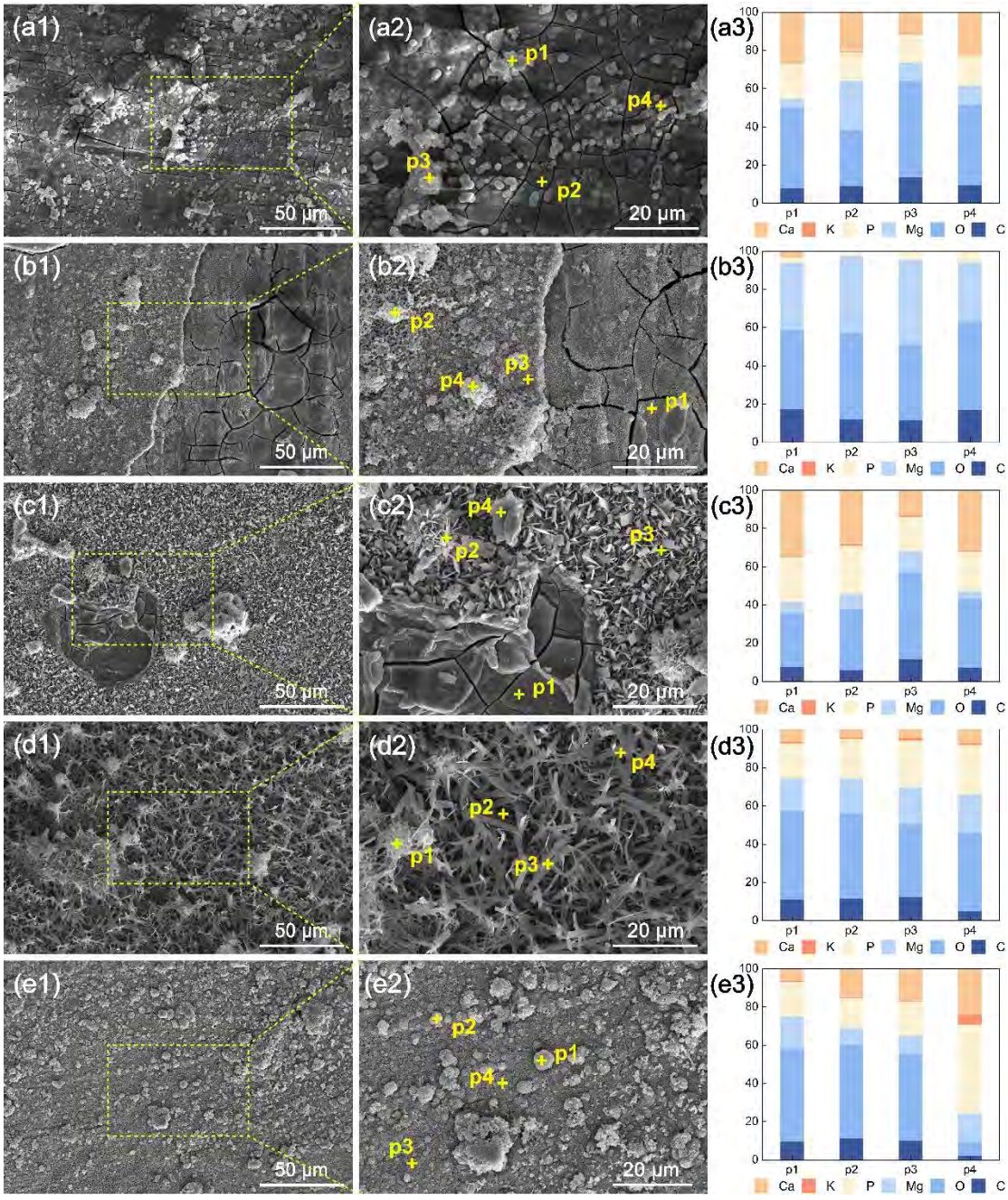

Fig. S1 SEM images and corresponding EDS results of (a1-a3) bare Mg, (b1-b3) MKP90, (c1-c3) MKP120, (d1-d3) MKP150, and (e1-e3) MKP180 after immersion in HBSS for 14 days.